LANGMUIR

pubs.acs.org/Langmuir Article

# Effects of Carbon Templates in Tetraethyl Orthosilicate-Derived Superhydrophobic Coatings

Joshua Goulas, Zizhou He, Philip Wortman, Kenneth J. Gordon, Cameron Romero, Blake Foret, April Bourlet, Thu Hoai Nguyen, Hui Yan, Mehdi Mokhtari, Hongmei Luo, Ziyang Zhang, and Ling Fei*

Cite This: *Langmuir* 2023, 39, 5495−5504 Read Online

ACCESS | Metrics & More | Article Recommendations | Supporting Information

**ABSTRACT:** Superhydrophobic coatings have garnered significant research interest due to their potential applications in areas such as ant-icing and windows. This study focuses on the development of superhydrophobic coatings using air-assisted electrospray and the effect of different carbon additives as templates in the coating. Carbon templates, with their unique topological varieties, offer a cost-effective alternative to other patterning technologies such as photolithography. By introducing dispersed carbon black, carbon nanotubes, and graphene additives in TEOS solution, silica is given the ability of localized secondary growth on or around the carbon surfaces as well as the building structure to provide adequate roughness on the substrate surface. The templated silica formations provide a thin coating with nano-scale roughness for heightened water resistance. As compared with the template-free coating that has small silica particles, a surface roughness of 135 nm, and a water contact angle (WCA) of 101.6° (non-superhydrophobic), the carbon templating effect allowed for increased silica particle size, a surface roughness as high as 845 nm, a WCA above 160°, and the ability to maintain superhydrophobicity over 30 abrasion cycles. The morphological characteristics that resulted from the templating effect correlate directly with heightened performance of the coatings. Herein, the carbon additives have been found to serve as cheap and effective templates for silica formation in thin TEOS-derived superhydrophobic coatings.

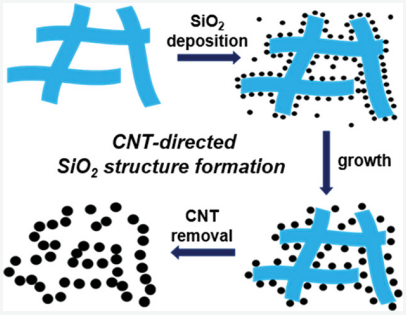




## 1. INTRODUCTION

In recent years, advancing technology and a determined scientific community have driven the innovation of new or advanced materials that serve specialized purposes to meet our ever-increasing needs and expectations of specialized materials. A rapidly developing area of advanced materials is superhydrophobic coatings, which can be easily applied and maintained on solid surfaces. Superhydrophobic surfaces are those that can sustain a water contact angle (WCA) of 150° or greater. An effective and robust coating can have incredibly useful benefits regarding cleanliness, surface protection, and other active functionalities. A large potential market for superhydrophobic coatings is corrosion-resistant layers that prevent structural integrity issues, improving safety and decreasing continuous capital costs.[1] Superhydrophobic coatings would aid in corrosion resistance not only in the presence of water but also acids and bases, which could be employed in many industrial applications. Superhydrophobic coatings applied to wire mesh or sponges can act as an oil−water separation mechanism for environmental and industrial applications.[2,3] Additionally, these coatings can be applied to a wide range of prominent fields and applications such as lenses, solar panels, windows, steel structures, boats, and vehicles among many others.[4−8]

Superhydrophobic coatings are generally created by a nanoscale hierarchical roughness that allows for peaks and troughs that trap air, preventing water or other liquids from contacting more than only the surface peaks.[9−11] In addition to structural roughness, low surface energy is the other requirement for superhydrophobic coating. Such coatings often involve the use of materials for surface structure design and control such as $SiO_2$ due to the higher optical transmittance.[12] Because $SiO_2$ is actually a hydrophilic material, a commonality among many newly developed $SiO_2$ superhydrophobic coatings involves the use of a low surface energy modifier such as perfluorooctylsilane.[13] With the ability to actively lower the surface energy of coatings through fluorinated agents, the major challenge then becomes the ability to control surface structures to increase the effectiveness of the coating, while also maintaining good adhesion and mechanical properties and, in some applications, high optical transparency.

Superhydrophobic coatings can be prepared by a variety of methods including sol−gel method,[14] dip-coating,[11] electrospinning,[15] and vapor deposition.[16] Many of these conventional approaches successfully produce superhydrophobic

Received: January 25, 2023
Revised: March 23, 2023
Published: April 5, 2023





https://doi.org/10.1021/acs.langmuir.3c00233
*Langmuir* 2023, 39, 5495−5504

surfaces with excellent self-cleaning performance and sufficient mechanical robustness against harsh environmental conditions. However, they often involve complex chemistry and tedious/time-consuming procedures or result in unfavorable surface characteristics. Recently, we reported an efficient air-assisted electrospray method for superhydrophobic coating fabrication, which allows for an easy, versatile, and consistently coated surface with great control over thickness and other parameters.[17] In this air-assisted electrospray method, the solution is loaded into a syringe pump and sprayed coaxially with air from an outer annulus onto the desired substrate. The solvent is evaporated during the spraying process, and thus, this method also significantly alleviates the surface cracks. In our previous work, commercial silica particles were dispersed directly into the coating solution, electrosprayed onto a surface, and post-treated to form a nano/microstructure that provides the required surface roughness.[17] Although a superhydrophobic surface with good self-cleaning function was obtained, the direct use of $SiO_2$ that is randomly dispersed in solution and then randomly packed on the substrate has limited control over the formation of the roughness-contributing structure. Additionally, the premade silica particles are loosely packed on the substrates, which affects the coating durability. To further improve the coating quality, it would be better to synthesize silica with controlled size and morphology to gain control over the roughness structural pattern. Therefore, in this study, silica sol−gel synthesis method will be used in the coating solution for better adhesion and durability. The carbon templating method will be adopted for better microstructure control.

Carbon of various structures and functional surfaces as well as with easy removal by thermal treatment is considered a great template material. Some coatings have utilized diverse types of carbon for the creation of superhydrophobic coatings such as carbon build up of candle soot[18] and carbon nanotubes by templating effects.[19−22] However, none of the reported works comprehensively studied the effect of different carbon (i.e., morphology) on the roughness and other properties on coating. Herein, different carbons, including 0D carbon spheres, 1D carbon nanotubes, and 2D graphene are studied systematically throughout this work. It was found that the key factors that improve the performance and characteristics of the coating in all cases are directly related to increased amounts of dispersed $SiO_2$ particles of 500 nm or larger, as they potentially induce larger surface roughness. This study develops relationships and highlights the key performance factors of controlled $SiO_2$ synthesis of tetraethyl orthosilicate from carbon-directed packing for coating application.

## 2. MATERIALS AND METHODS

**2.1. Materials.** Polyacrylonitrile (PAN) ($M_W$ 150,000), tetraethyl orthosilicate (TEOS), ammonium hydroxide (28−30%), and trichloro(1H,1H,2H,2H-perfluorooctyl) silane (PFOCTS) were acquired from Sigma−Aldrich. Dimethylformamide (DMF) was obtained from VWR. Carbon black was obtained from Gelon Lib Group. Multiwalled functional carbon nanotubes were obtained from SkySpring Nanomaterials. Graphene was obtained from Graphenea. All materials were used without further purification for the synthesis of the superhydrophobic coatings.

**2.2. Preparation.** The preparation of superhydrophobic coatings began with the solvent solution in which 5 mL of DMF was added to the sample vial in addition to 50 mg of PAN. The solution was set in a 70 °C oven for a minimum of 1 h to totally dissolve all polyacrylonitrile into the DMF solvent. A variable amount of carbon (0−50 mg at 5 mg increments) was then added into the PAN/DMF solution and subjected to ultrasonication for 1.5 h to fully disperse the particles. Once ultrasonicated, the samples were magnetically stirred while adding 200 microliters of TEOS followed by 400 microliters of ammonium hydroxide. The samples were then left to stir for 24 h. Afterward, the samples were prepared via air-assisted electrospray utilizing a similar setup as electrospinning. The coating was sprayed through a coaxial needle in which the coating solution was dispersed from the inner needle and assisted by the air sprayed through the outer annulus. The electrospray conditions consisted of a voltage of 20 kV, infusion rate of 30 microliter per minute, air flowrate of 4 liters per minute, and a distance of 15 cm from the spray tip to the substrate. The solution was sprayed onto clean glass slides and then placed into an open atmosphere tube furnace at 600 °C for 1.5 h. The ramp rate of the tube furnace was 2 °C per minute to prevent any deformation of glass slides. After annealing, all carbon within the sample was combusted and removed, leaving a thin layer of $SiO_2$ coating. Once the carbon was removed, the samples then underwent chemical vapor deposition within a vacuum chamber with 40 $\mu$L of PFOCTS placed in the vessel with the samples and then heated to 80 °C for 30 min under vacuum. The PFOCTS vapor then settled onto the sample, lowering the surface energy of the coating, thus providing a superhydrophobic surface.

**2.3. Characterization.** The samples underwent a variety of tests to detail the effectiveness of the coating and also highlight key characteristics of the surface structure. Scanning electron microscopy (SEM, Scios 2 DualBeam) was used to investigate the morphologies. Before generating images captured by SEM, all samples were gold-sputtered under high vacuum conditions with a sputter coater to improve the electrical conductivity of the coatings. The WCA was measured with a Kruss Drop Shape Analyzer. The static WCA for each sample was measured with approximately 2 $\mu$L droplets at various locations across the surface and displayed as the mean value of measurements along with the standard deviation. WCA results are displayed in terms of degrees. Through SEM imaging, the surface structures were observed. For the purposes of this research, all particles exceeding 500 nm in diameter were counted and displayed as data in terms of particles per square micrometer. This allows for an estimate of the surface particle distribution as well as a key comparison in relation to the WCA for each specific sample. The surface of the coating was also characterized by atomic force microscopy (AFM) to detail the topology of the structure such as the average roughness. Sample transparency was measured via ultraviolet to visible light (UV−vis) spectrum transmittance, to further assess and compare the coating distribution in correlation with observed particle size, roughness, and static contact angle performance. The coated samples were also subject to abrasion cycle testing to determine the coating durability between the three carbon templated surfaces. Each cycle consists of one sweeping motion across the entirety of the surface with a microfiber cloth and a 16-ounce weight to maintain uniformity across all cycles and samples. Each sample's WCA was measured prior to abrasion testing to establish a baseline for testing and compare with the results after abrasion cycles.

## 3. RESULTS AND DISCUSSION

**3.1. Carbon Template.** Each carbon template type has a distinct structure and characteristics that can potentially play an important role in the local growth and nucleation of TEOS-derived silica in the solution. As seen in Figure S1, images of the bulk carbon templates allow for visualization of aggregate tendencies of each carbon type. EDS analysis confirmed that carbon and oxygen are the only elements present in carbon additives. BET surface measurements were also conducted for each carbon template type and are summarized in Table S1. Both 1D CNT and 2D graphene show increased surface area than that of the 0D carbon black primary particles. When the bulk carbon is dispersed in the solvent (DMF), a majority of the aggregates will unwind or untangle themselves, where the


https://doi.org/10.1021/acs.langmuir.3c00233
Langmuir 2023, 39, 5495−5504

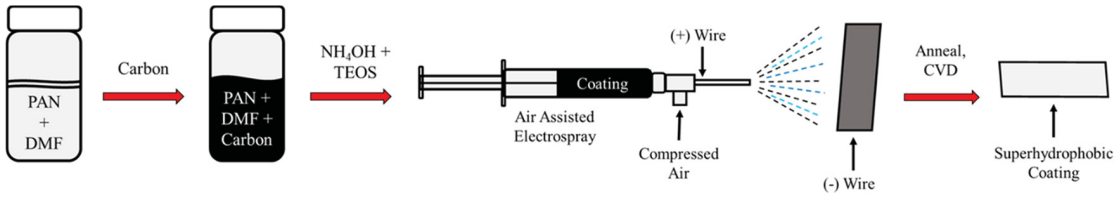


**Figure 1.** Schematic of the coating preparation process.

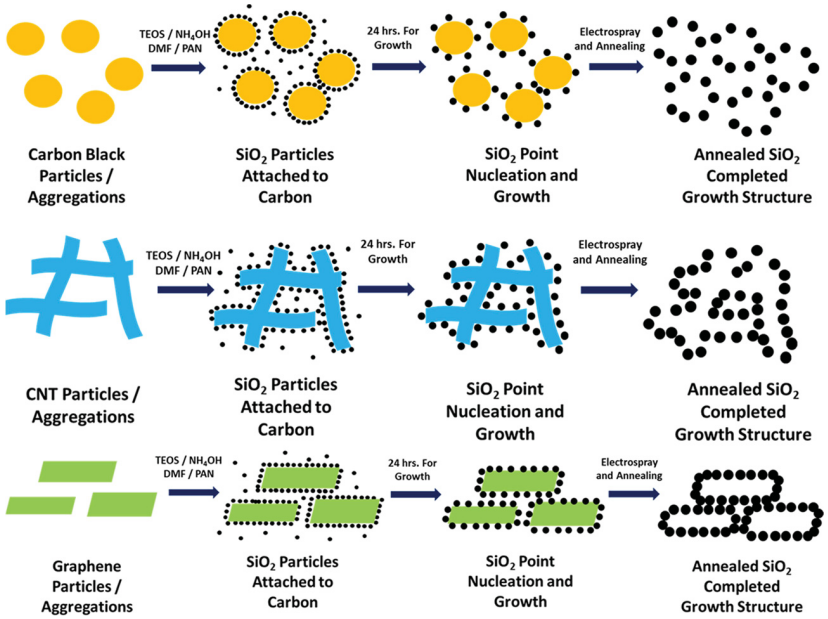


**Figure 2.** Schematic of the carbon templating effect through the coating process.

individual morphologies and properties tend to be important for templating effect. Due to the individual characteristic shapes and properties of carbon black (0D), carbon nanotubes (1D), and graphene (2D), each will lead to different effects on the surface structure of the coating.

**3.2. Stöber Reaction Method for $SiO_2$ Synthesis.** With the intentionally selected carbon template, $SiO_2$ will be grown in situ. The Stöber reaction method has been a popular method for producing controlled $SiO_2$ from TEOS. It is generally based upon the reaction of TEOS in the presence of an alcohol with ammonia as an aqueous catalyst to drive the hydrolysis and condensation two-part reaction.[23] The overall reaction is as follows:[23]

$$Si(OC_2H_5)_4 + 2H_2O \rightarrow SiO_2 + 4C_2H_5OH \quad (1)$$

The basic Stöber reaction involves the two-step process that begins with a hydrolysis reaction in which the interactions of hydroxyl anions and the TEOS molecules produce silicic acid that then proceeds into a condensation reaction. The acid interacts with other ethoxy groups or more hydroxyl groups leading to the condensation of both water and ethanol.[23] Though the reaction is also dependent on water and no pure water is added into the reaction mixture, water is provided by the aqueous ammonia solution. The overall reaction has been determined to be first order with respect to TEOS and co-dependent on both the produced water concentration and ammonia concentration.

$$-\mathrm{rTEOS} = k[\mathrm{TEOS}][H_2O]_x[NH_3]_y \quad (2)$$

The typical overall rate law for the reaction can be seen above in eq 2.[24] An interesting measure regarding this experiment is that the common alcoholic solvent typically involved in Stöber kinetics is replaced by DMF, a polar, aprotic, non-alcoholic solvent. DMF was used in the solution which has been shown to decrease the effects of cracking on thin films of silica networks derived from sol−gel synthesis.[25]

Particle size and distribution are key to many applications. In the case of coatings, the silica size is also critical, as it directly relates to surface roughness. In our reaction, the rate-limiting reactants are held constant, and hence, the diameter of silica particles from the Stöber reaction process is controlled by the relative contribution from nucleation and growth processes. Therefore, in this work, different carbon templates are used to guide/tune the nucleation and growth process. For all purposes of this experimentation, concentrations of TEOS and ammonia are held constant, while varying carbon concentration, which is presumed to not affect the actual reaction rate but allow for increased particle growth through offering surface nucleation sites.

In addition, the continuously stirred reaction vessels are allowed 24 h to react with an assumed fast reaction rate; therefore, $dN_{TEOS}/dt$ (change in moles of TEOS) approaches zero over the allotted time. This is to bring common and steady reaction products for each of the samples as well as allow time for particle nucleation and growth.

**3.3. Coating Fabrication.** The overall fabrication process is briefly summarized below in Figure 1. PAN polymer solution is prepared first, and then, carbon is well dispersed by ultrasonication. Ammonia and TEOS are then added while


https://doi.org/10.1021/acs.langmuir.3c00233
Langmuir 2023, 39, 5495−5504

stirring and left to react for 24 h. The prepared solution is then coated on the substrate via air-controlled electrospray, which has been introduced in our previous work.[17] Within the spraying process, all spray parameters are kept consistent to avoid deviation or variation between coatings so that the observed sample variance is from different carbon templates. The obtained coating was then followed by heat treatment to remove the carbon template from the coating, resulting in a transparent or translucent coating. The coating then undergoes vapor deposition of fluorosilane to effectively reduce the surface energy of the newly formed roughness structure, together leading to a superhydrophobic coating.

Silica growth in sol−gel synthesis can be characterized by a combination of monomer addition[26,27] and particle aggregation.[28,29] Rahman et al. explains that silica particles undergo two stages of growth, in which primary particles nucleate throughout the reaction and these particles then form aggregations among themselves, which can create larger networks.[30] In this present work, it was hypothesized that introducing a medium to allow for point nucleation and aggregation to the reaction mixture would allow for increased particle size and a templating effect for aggregate silica. The effect of different carbon templates on $SiO_2$ formation, arrangement, and thus roughness control of coating is proposed in Figure 2. Different carbon types provide distinctly different surface shapes and patterns of stacking aggregations. As carbon templates are introduced into the solution, TEOS reacts to form silica particles around the carbon templates. During the formation of silica, particles undergo secondary growth forming larger particles adhered to carbon. Once electrosprayed onto the substrate, the samples are annealed to remove the carbon template, leaving behind a patterned silica formation.

Noteworthily, with increasing carbon concentration within the coating solution, the suspended surface area becomes larger as the mass ratio of carbon increases. The effects of increased surface area of carbon can be both positive and negative in terms of particle growth and performance. Lack of sufficient surface area leads to insufficient nucleation and particle growth sites, resulting in poor coating performance. When the surface area of the carbon template becomes too large, particles tend to have an abundance of area to grow, which can also result in lack of particle formation into large enough particles due to decreased proximity of silica particles on carbon surfaces. Higher concentrations of carbon with a large surface area within the solution also tend to be performance limiting in which the abundance of carbon surface area prevents increased adhesion of silica to the substrate. Namely, there is an optimal range of carbon mass ratio. Therefore, different ratios of carbon additives were also studied for each template.

**3.4. Coating Surface Morphology and Particle Size.** In the Stöber process of silica formation, particles are formed from the combination of reaction parameters as well as different step growth. Blaaderen et al. details the growth mechanisms of silica from tetra alkoxysilanes, in which the particle size is independent of aggregation and heavily dependent upon the concentrations of ammonia and water but is determined by a local growth mechanism. There is also an explanation that ions, apart from reactant concentrations, can affect the particle size, in which the solution gains colloidal stability and the growth ends.[31] In this study, there is no presence of ions but there is a suspended carbon additive that allows for localized growth until the solution reaches stability. There are arguments that silica growth is only dependent on reactant concentrations and pH; however, Lee et al. details that aggregation growth cannot be ruled out with the successful prediction of an aggregation model.[32] Here, this study has shown through SEM microscopy that the addition of a carbon substrate to a Stöber reaction medium allows for enhanced aggregation from localized growth in solution. This is likely due to intermolecular interactions between the silica and the carbon within the polar organic solution. Sharaf et al. briefly discusses the effects of surface modification to $SiO_2$ particles that provide a degree of organophilicity to adjust particles' behavior and interaction.[23] A possible explanation for the influence of carbon additives is the degree of organophilicity of $SiO_2$ particles, in which the carbon additives attract silica and allow for continued growth of particles as well as adherence to the carbon template, providing a patterned structure. This assumption would shed light on how carbon additives affect a coating in which the reaction is independent of carbon. Through SEM imaging, it has been determined that directing $SiO_2$ growth by introducing a carbon reaction medium for promoting crystal nucleation does indeed greatly affect the particle size and distribution as well as the performance of the coating.

Control samples were first studied to determine surface characteristics in the absence of key coating constituents. A control sample with the absence of the ammonium hydroxide catalyst solution and carbon, seen in Figure 3a,b, does not create any continuous silica coating nor develop a well patterned surface structure. The surface contains only crystalline deposits from TEOS that are sparsely distributed. Figure 3c,d details the surface of the coating without the addition of any carbon in the reaction solution but with the presence of ammonium hydroxide catalyst solution. With ammonia available for catalyzing the reaction, silica particles are now formed. SEM imaging shows the overall surface including cracks in the coating layer, exposing the bare substrate with a minimal surface structure and relatively smooth layers of nano-silica. Figure 3d shows the thickness of the surface coating, illustrating the compact silica particle

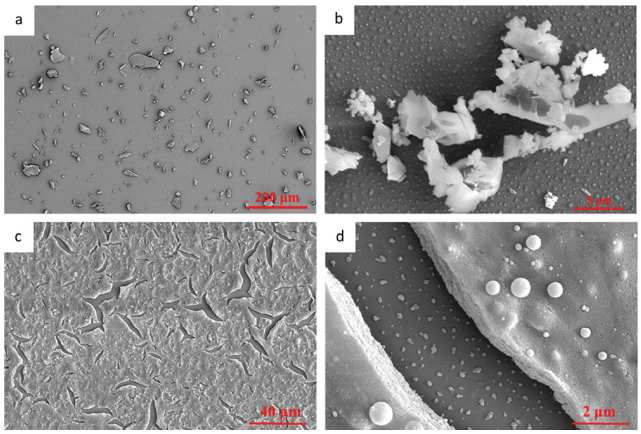


**Figure 3.** SEM images of coating control samples. Absence of ammonium hydroxide control: (a) low-magnification surface morphology, (b) crystalline deposition. Absence of carbon control (with presence of ammonium hydroxide): (c) low-magnification surface morphology detailing surface cracks, (d) surface crack displaying a layer of nano-silica comprising the coating.


https://doi.org/10.1021/acs.langmuir.3c00233
Langmuir 2023, 39, 5495−5504

composition. With no carbon in the reaction mixture, the silica particles lack structure and ability for growth into required roughness, leading to a relatively smooth structure that has no heightened superhydrophobic abilities.

In order to understand the performance of the superhydrophobic coatings, it is important to examine the surface morphologies of the coatings. A large factor in the performance of the coatings is the surface roughness and structural distribution over the substrate. Since the coating is annealed, removing the carbon and some of the surface structure, it is important to understand the physical characteristics of the coating both before and after the annealing process. Figure 4

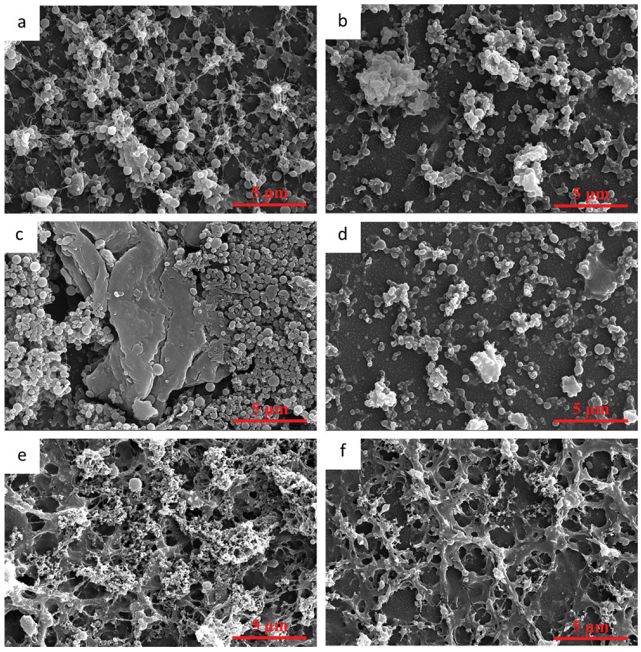


**Figure 4.** SEM imaging of 20 mg of carbon samples of pre-annealed (a) carbon nanotubes, (c) graphene, (e) carbon black, and post-annealed coating from (b) carbon nanotubes, (d) graphene, and (f) carbon black.

above depicts the surface morphology of the coating before and after annealing for each type of carbon additive. In each of the coating samples, it is evident that the annealing process removes a significant amount of the surface structure, allowing for sufficient roughness. In comparison, the carbon black sample in Figure 4e is shown to have a very complex surface structure as compared to the other carbon additive. After the annealing process, the surface (Figure 4f) remains rather dense and complex with tight gaps and a lack of larger gaps between surface peaks, which will potentially result in an elevated surface roughness. This could be due to the fact that carbon black particles tend to form aggregates of random shapes with many small gaps in the surface structure that allows an abundance of silica precursors to penetrate in for surface adhesion to the substrate, and thus, a larger portion of the coated surface is covered with layers of continuous nanosized silica network that is not removed during annealing, which potentially leads to larger roughness and thickness. In the case of $CNT_S$, they randomly interlock with each other to create a carbon network that provides nucleation sites for $SiO_2$ growth, and the spaces among the network allow for silica growth, forming an effective template. As shown in Figure 4a, carbon nanotube-templated coating indeed tends to have many spherical silica growing along with the CNT strands or networks. The CNT coating after annealing (Figure 4b) also shows an evenly distributed surface structure, which has sufficiently spaced large particles and clusters that result in a decreased or less dense surface roughness from that of the carbon black coating. The graphene coating, shown in Figure 4c, details the large carbon aggregates surrounded by many silica sphere aggregations on the surface. After annealing, the large carbon aggregates are removed (Figure 4d). The graphene sample appears to have the most significant surface transformation during the annealing process, which can be attributed to the 2D sheet effect with very high surface area in which graphene sheets occupy a large portion of the substrate preventing silica adhesion. The portion of unadhered silica particles that are not directly in contact with the substrate (i.e., on the surface of graphene) are also removed during annealing. Due to the loss of unadhered silica, the surface coating becomes much like that of the CNT coating, although the silica distribution around graphene seems denser before annealing (Figure 4c) than that of CNT-templated samples (Figure 4a). In conclusion, these surface structures and different packing effects (i.e., 0D carbon particles piling, 1D CNTs interwinding, and 2D graphene sheets stacking) of the carbon templates are directly related to the physical characteristics of each carbon template. Through cross section analysis, the average obtained coating thickness after the removal of 20 mg of each carbon was 3.7 $\mu$m for carbon nanotube-templated sample, 4.4 $\mu$m for graphene, and 6.3 $\mu$m for carbon black. Due to carbon templating, these thicknesses are a drastic improvement in decreased thickness and pattern effect from our previous work in which a coating thickness of 28.2 $\mu$m was observed by using commercial $SiO_2$ particles that can only randomly and loosely pack on the substrate.[17] Due to the differences in surface structures caused by carbon templating, each template type produces a different surface roughness that corresponds to the dispersion of larger particles and as well as light transmittance data seen later in this section.

Through AFM characterization, the surface roughness of each carbon templated coating along with the control sample are shown in Figure 5. Each of the three carbon templates produced a varied surface roughness, all of which are substantially larger than that produced by the control coating (no carbon) at an average roughness of 135 nm. The largest roughness (average of 845 nm) was produced by the carbon black template as expected when analyzing the pre-annealed and post-annealed silica aggregations through SEM. With the packing effect of different dimensional carbons, graphene provided a much lower roughness averaging 526 nm with the carbon nanotube coating closely behind at an average roughness of 395 nm.

As the roughness of the coating is crucial for superhydrophobicity and, here, mainly the silica particles are the contributing factor for roughness, it would be beneficial to correlate the roughness with the silicon particle size for each sample. From the previous SEM images, large spheroid particles can be easily distinguished from the rest of the structure seen in the images. It has been found that others have investigated the particle size effects on the performance of coatings and found interesting results. Heiman-Burstein et al. found that when examining the WCA of various ratios of TEOS:ODTMS (octadecyltrimethoxysilane), each ratio had a different average particle diameter with different WCAs. The


https://doi.org/10.1021/acs.langmuir.3c00233
Langmuir 2023, 39, 5495−5504

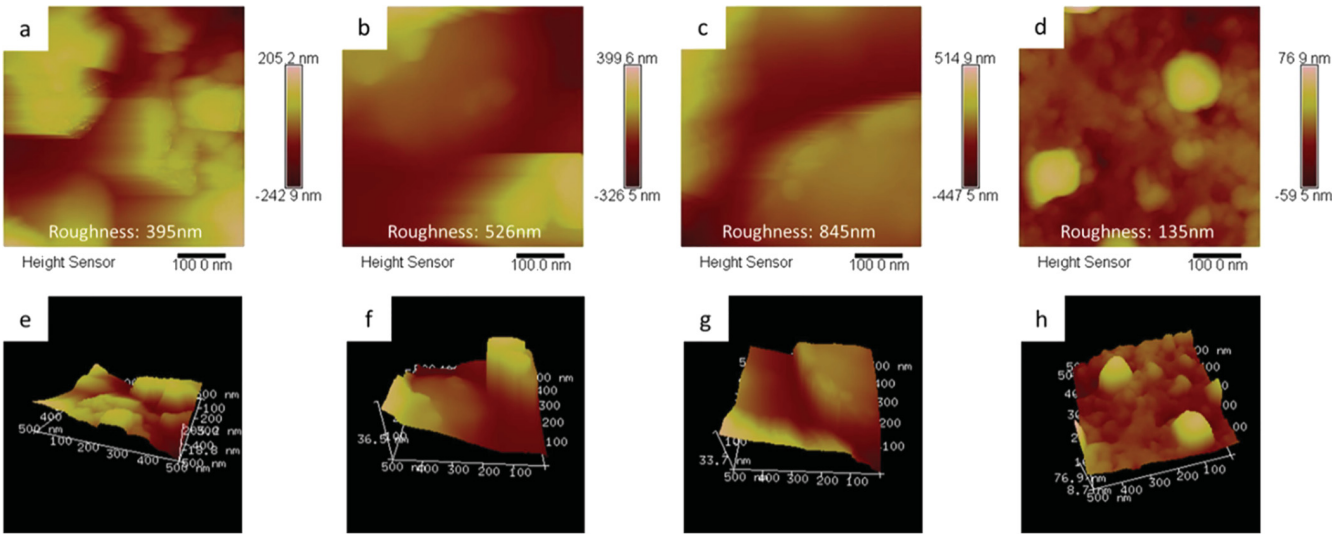


**Figure 5.** Atomic force microscopy (AFM) images of coating sample surfaces illustrating surface roughness. The 2D images of annealed coating samples are as follows: (a) 20 mg of carbon nanotubes, (b) 20 mg of graphene, (c) 20 mg of carbon black, and (d) control coating (no carbon). The 3D images of annealed samples are as follows: (e) 20 mg of carbon nanotubes, (f) 20 mg of graphene, (g) 20 mg of carbon black, and (h) control coating (no carbon).

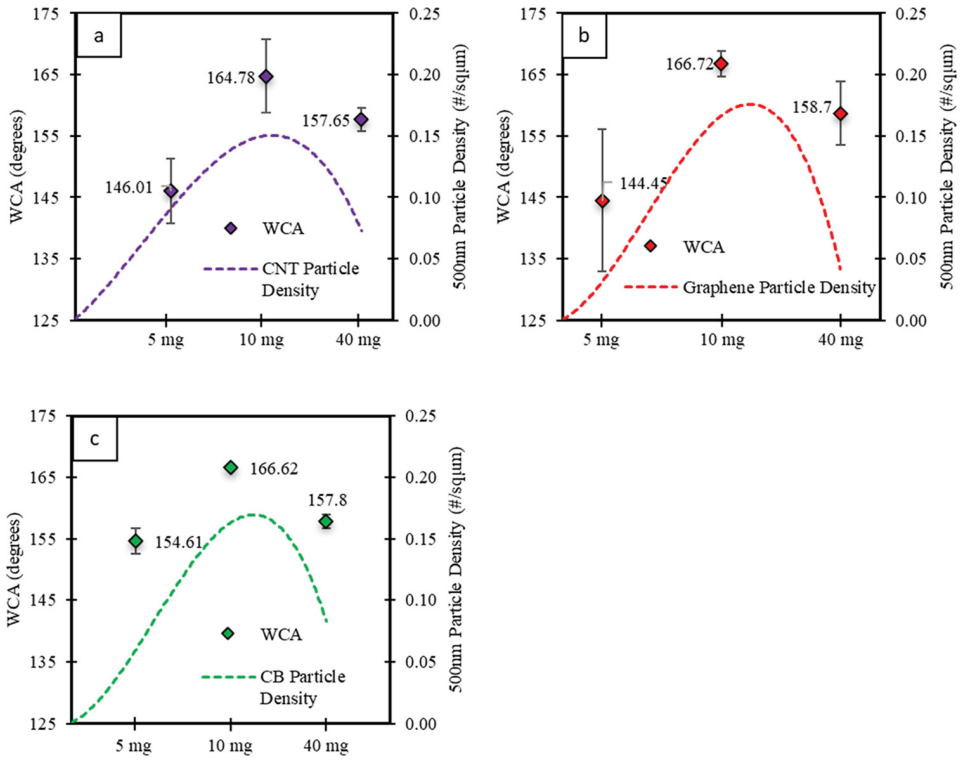


**Figure 6.** Particle trend-correlating WCA of the coating (after thermal treatment) and the number of 500 nm or larger particles per square micrometer: (a) carbon nanotubes, (b) graphene, and (c) carbon black.

sample that had proven to reach most favorable characteristics had an average particle diameter of 455 ± 267 nm.[33] Therefore, for correlation purposes, particles around 500 nm were selected as the key identifier among the coatings and are detailed in green in the SEM images for 5, 10, and 40 mg of each carbon in Figure S2.

Displayed in Figure S2 are the visible differences in the surface morphology of the different carbon-directed coatings at different amounts of additives. In Figure S2a, d, and g, carbon nanotubes appear to direct the surface in a wavy, nearly fibrous appearance likely due to the overlapping and entangling of the long carbon nanotubes, which allows for adequate gaps in the surface without excessive aggregation. The graphene-directed coatings (Figure S2b, e, and h) appear to show large sheet-directed $SiO_2$ aggregates, consistent with the typical shape and tendency of graphene to form large layered packing. Carbon black at low amounts (Figure S2c) does not show that much difference from other two carbon-templated coatings, but at higher ratio (Figure S2i), it shows more fine aggregates with smaller gap in between than that of the coatings from the other


https://doi.org/10.1021/acs.langmuir.3c00233
Langmuir 2023, 39, 5495−5504

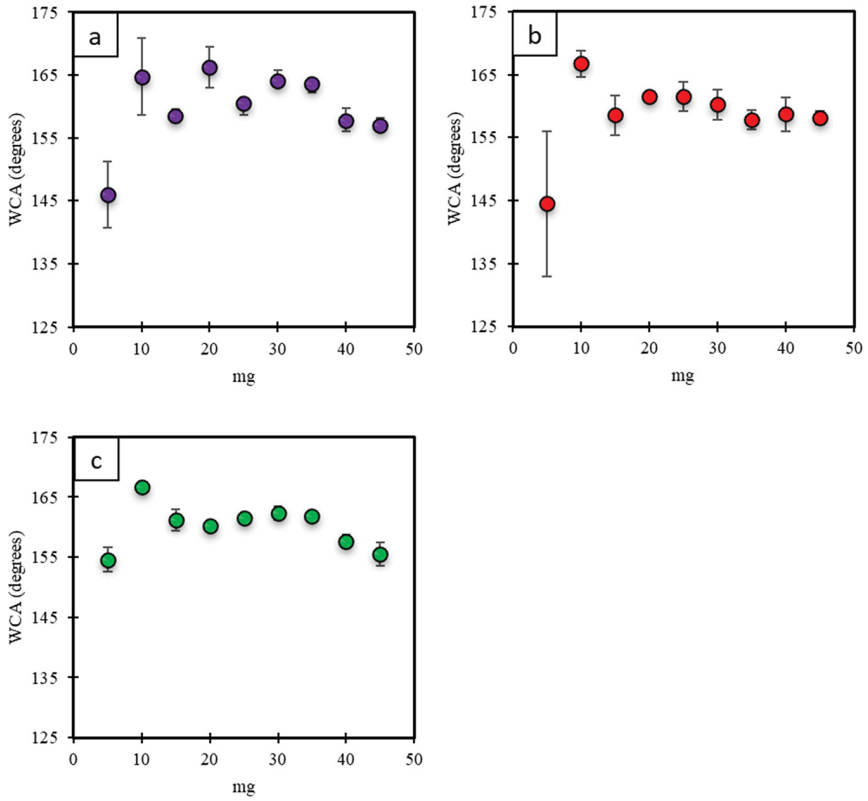


**Figure 7.** Static WCA vs mass of carbon categorized by carbon type: (a) WCAs of carbon nanotubes, (b) WCAs of graphene, (c) WCAs of carbon black (some data points do not show obvious standard deviation as it is too small to see).

two carbon-templated coatings, in accordance with the trait of particle-to-particle packing. In all cases, the 10 mg carbon-coated samples seen in Figure S2d–f clearly have the largest amount of spheroid particles on the surface. This behavior is consistent with the hypothesis that the carbon in the reaction solution serves as a point of nucleation. When the carbon amount is too small, the nucleation sites are limited, leading to a small number of large particles and three samples sharing a similar morphology. When the carbon amount is very high, there are surplus nucleation sites that also leads to smaller particle formation in a network way as the carbon template packing becomes more continuous. Namely, there are simply many small particles as opposed to growing large particles. It is also observed that as the carbon template concentration increases, the packing effect of different carbon templates becomes more clear, leading to a more distinguished surface morphology.

The dispersity of larger particles is highly possible to affect the overall surface roughness and thus superhydrophobic properties of the coated surface. To understand the surface morphology to the actual performance of the coatings, 500 nm or larger $SiO_2$ particles were counted and are tabulated as particles per square micrometer. These particles were counted by analyzing different areas of the surface for each carbon and concentration and then dividing the number of 500 nm or larger particles by the image area. The amount and distribution of larger particles on the performance of the superhydrophobic coatings is detailed in Figure 6.

Analyzing Figure 6 of WCA and the large particle surface density, there is an apparent convex behavior of the number of 500 nm particles with increasing carbon concentration. From zero carbon, the number of large particles increases to a maximum and then begins decreasing as sharply as it arose, following the same trend of the number of large particles in these different carbon templates. Another interesting detail that can easily be overlooked is the correlation between the WCA standard deviation and the number of large particles in a particular concentration subset. For instance, for each of the 5, 10, and 40 mg sample sets, the carbon sample with the lowest number of large particles in that subset also has the largest standard deviation. This could be a signal that lower concentrations of carbon templates lead to a more discrete distribution of larger aggregations. It is also observed that carbon black-templated coatings have the smallest standard distribution of the WCA across different additive amounts among the three sets of samples, indicating that 0D particle-to-particle packing tends to be more isotropic. The number of large particles in each sample also closely correlates with the actual WCA performance.

**3.5. Surface Wettability.** When assessing the performance of the individual carbon types in the superhydrophobic coatings, a control baseline was established for performance of the control coating with zero carbon additive. Shown in SEM in Figure 3c, it only achieved a WCA of 101.6°, nearly 50° under superhydrophobicity. It is abundantly clear that the performance of the coatings is drastically increased by the addition of carbon to the reaction solution. Given that there was no carbon in the sample to allow thorough nucleation and growth of $SiO_2$ into many large particles and surface structures, the WCA performance of the coating suffered. The images of a water droplet on bare glass and carbon nanotube-templated coating are shown in Figure S3 for direct comparison. The static WCAs of coating templated by various carbon samples at various concentrations are shown in Figure 7.


https://doi.org/10.1021/acs.langmuir.3c00233
Langmuir 2023, 39, 5495−5504

The overall performance of each carbon additive type is similar in which they each reach and maintain a superhydrophobic level of performance or a WCA greater than 150° with a sliding angle less than 5°. It is abundantly clear that the performance of the coatings is drastically increased by the addition of carbon to the reaction solution. There is a maximum WCA achieved for each of the carbon samples, and from there, the sample WCAs begin to slowly decrease. This can be explained by comparing the WCA data with SEM imaging and large particle density analysis. As carbon content increases from zero, surface area is provided that allows for nucleation and local aggregate growth, resulting in templated fine silica structures. As carbon content further increases, the silica particles have sufficient template surface area for enhanced local growth resulting in larger particles and less fine silica as evident through SEM. Once carbon content has become high, there is an abundance of the template surface area, and silica particles have less ability to undergo local growth, which again results in very fine silica creating complex structures. In the range of optimum local growth, the highest amount of larger particles is formed, leading to higher contact angles. We also estimated the samples' surface energy, following the previous work by Zhang et al., where the Owens−Wendt−Kaelble (OWK) method was utilized.[34] In detail, the contact angles of two liquids (i.e., water and ethylene glycol) were measured and plugged into the OWK equation. For all samples, the surface energy is around 20 mN/m. It could be all samples coated with the same fluorinated polymer.

**3.6. Light Transmittance.** The transparency and superhydrophobicity are mutually exclusive, which means that higher rough structure leads to light scattering and thus, it reduces transparency. Transmittance data of the coated samples can provide additional information into the correlation between templated roughness and dispersion. The samples were analyzed based on their transmittance of wavelengths from 300 to 900 nm. These samples were chosen from low concentration compared with high concentration of carbon to detail the effects of particle size on relative transparency. The results of UV−vis transmittance can be seen in Figure S4.

The results of UV−vis measurements coincide with the SEM imaging results in terms of mass aggregation and higher roughness with higher carbon content. As discussed previously and shown in Figure 4, the carbon black coating remained highly complex after annealing with a large surface structure as compared to graphene and carbon nanotubes. This result is also seen here through transmittance data. Carbon black-templated coatings maintained a relatively lower transmittance across each tested carbon concentration and continuously decreased as the concentration increased. The results of UV−vis measurements can also confirm the immense stacking of particles on the surface of higher concentration carbon black coatings as shown by the lack of transmittance across the spectrum as compared to graphene and carbon nanotube-templated coatings.

The transmittance of the CNT and graphene coatings both increase from 10 to 25 mg before reducing at higher concentrations likely due to the decreased formation of larger particles, leaving the surface covered in a complex network of finer silica particles. Carbon nanotubes provided the most transparent coating from the range of 10−25 mg of carbon in the precursor solution. Additionally, the order of transmittance matches directly with the order of surface roughness from AFM as well as thickness of the coatings from different carbon templates.

**3.7. Durability.** Durability is another important factor for coating, which is the ability of the material to withstand abrasion as well as harsh environments. In the durability study, coatings templated from 25 mg of the carbon black, graphene, and carbon nanotube were subjected to repeated abrasion cycles, and their performance was evaluated at 10 cycle intervals. Each sample's WCA was measured prior to abrasion testing to establish a baseline for testing, and the results of abrasion cycles can be seen in Figure 8. After 10 abrasion cycles, the performance of the carbon black sample increased from 160° to 164°, which can be explained by the removal of loose silica on the surface of the sample, exposing the more durable and adequately rough structure underneath the loose particles. While the carbon black sample remained much the same in terms of performance, the graphene sample experience a significant decrease from 160° to 125° within 10 cycles. It is possible that the large surface area of the graphene sheets simply assumes too much of the bare glass surface, impeding the ability of silica formation to adhere to the surface. The performance of the graphene coating further decreases with 20 cycles before leveling out at around 115°. The carbon nanotube sample reached a stable WCA after repeated cycles above 155°, while the carbon black sample remained above 160° through 30 abrasion cycles proving to be also more durable than graphene-directed coatings, indicating that the direct contact of silica to the substrate is critical for durability.

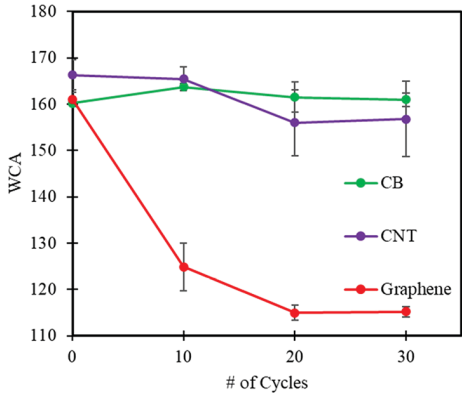


**Figure 8.** Water contact angle performance with repeated abrasion cycles for carbon black, carbon nanotubes, and graphene coatings.

In addition to abrasion cycle durability tests, the coating was subject to tests to determine the effects of acidic and basic environments. The coated samples were placed into 20 wt % caustic (NaOH) solution and 37 wt % HCl separately for 12 h. The acidic and basic solutions both had no effect on the coating performance. Figure 9 shows droplets of 20 wt %

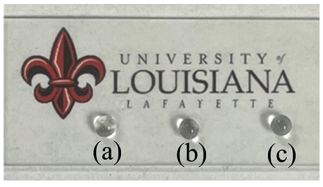


**Figure 9.** Image of a coated glass slide after annealing with droplets of (a) 20 wt % caustic, (b) water, and (c) 37 wt % HCl.


https://doi.org/10.1021/acs.langmuir.3c00233
Langmuir 2023, 39, 5495−5504

caustic, water, and 37 wt % HCl on the surface of the coating. The layer comprises only silica formations, and acid has no effect on the coated surface. Silica and NaOH can react at high temperatures; thus, the coating can still serve as a protecting layer at low or mild temperature settings. In addition, the fluorinated top layer on $SiO_2$ further extends its protecting effect in the harsh environment, making it applicable to many industrial settings, in which acids and bases are frequently used.

## 4. CONCLUSIONS

After analyzing characteristic effects of carbon additives into a controlled reaction mixture, it is evident that the amount and type of carbon have a distinct effect on the performance and surface morphology of the coating. Each of the carbon types certainly affected the particle size and performance, increasing the WCA from 101.6° of the control sample to above 150° and maintaining superhydrophobicity. It is evident that each of the carbon additives provides a sufficiently stable and dispersed surface structure, leading to an average WCA of over 155° over all carbon concentrations. Each carbon additive template produces different surface roughness as verified by AFM and leads to different light transmitting capabilities. When applying abrasion cycles to the coated samples, carbon black and carbon nanotube coatings maintained high durability, while the graphene coating experiences a significant decrease in performance due to poor surface adhesion. In conclusion, this work found that carbon additive templates are critical on particle nucleation and growth and surface structures in TEOS-derived superhydrophobic coatings, significantly boosting the superhydrophobicity of the coatings and affecting light transmittance and durability.

## ■ ASSOCIATED CONTENT

### Supporting Information

The Supporting Information is available free of charge at https://pubs.acs.org/doi/10.1021/acs.langmuir.3c00233.

SEM and TEM images of the carbon templates; BET surface area of the carbon templates; SEM images of post-annealed coatings with 500 nm particles selected in green; water droplet on surface images on bare glass and coated sample; and UV−vis comparison of coating (PDF)

## ■ AUTHOR INFORMATION


### Corresponding Author

**Ling Fei** − *Department of Chemical Engineering, University of Louisiana at Lafayette, Lafayette, Louisiana 70504, United States;* orcid.org/0000-0002-0954-5168; Email: ling.fei@louisiana.edu

### Authors

**Joshua Goulas** − *Department of Chemical Engineering, University of Louisiana at Lafayette, Lafayette, Louisiana 70504, United States*

**Zizhou He** − *Department of Chemical Engineering, University of Louisiana at Lafayette, Lafayette, Louisiana 70504, United States*

**Philip Wortman** − *Department of Petroleum Engineering, University of Louisiana at Lafayette, Lafayette, Louisiana 70504, United States*

**Kenneth J. Gordon** − *Department of Chemical Engineering, University of Louisiana at Lafayette, Lafayette, Louisiana 70504, United States*

**Cameron Romero** − *Department of Chemical Engineering, University of Louisiana at Lafayette, Lafayette, Louisiana 70504, United States*

**Blake Foret** − *Department of Chemical Engineering, University of Louisiana at Lafayette, Lafayette, Louisiana 70504, United States*

**April Bourlet** − *Department of Chemical Engineering, University of Louisiana at Lafayette, Lafayette, Louisiana 70504, United States*

**Thu Hoai Nguyen** − *Department of Chemical Engineering, University of Louisiana at Lafayette, Lafayette, Louisiana 70504, United States*

**Hui Yan** − *Department of Chemistry, University of Louisiana at Lafayette, Lafayette, Louisiana 70504, United States;* orcid.org/0000-0001-9279-5370

**Mehdi Mokhtari** − *Department of Petroleum Engineering, University of Louisiana at Lafayette, Lafayette, Louisiana 70504, United States*

**Hongmei Luo** − *Department of Chemical and Materials Engineering, New Mexico State University, Las Cruces, New Mexico 88003, United States;* orcid.org/0000-0002-9546-761X

**Ziyang Zhang** − *Kayaku Advanced Materials Inc., Westborough, Massachusetts 01581, United States*

Complete contact information is available at: https://pubs.acs.org/10.1021/acs.langmuir.3c00233


### Notes

The authors declare no competing financial interest.

## ■ ACKNOWLEDGMENTS

This research was funded by the NSF OIA-1946231 (CFDA #47.083) under contract number (2023)-LAMDATr2-07 and The Energy Institute of Louisiana. We also acknowledge support from Chevron Endowed Professorship in Chemical Engineering and NSF MRI Program (NSF-1920166).

## ■ REFERENCES


(1) Fürstner, R.; Barthlott, W.; Neinhuis, C.; Walzel, P. Wetting and Self-Cleaning Properties of Artificial Superhydrophobic Surfaces. *Langmuir* **2005**, *21*, 956−961.

(2) Xu, P.; Li, X. Fabrication of $TiO_2/SiO_2$ Superhydrophobic Coating for Efficient Oil/Water Separation. *J. Environ. Chem. Eng.* **2021**, *9*, No. 105538.

(3) Yu, H.; Wu, M.; Duan, G.; Gong, X. One-Step Fabrication of Eco-Friendly Superhydrophobic Fabrics for High-Efficiency Oil/Water Separation and Oil Spill Cleanup. *Nanoscale* **2022**, *14*, 1296−1309.

(4) Fei, L.; He, Z.; LaCoste, J. D.; Nguyen, T. H.; Sun, Y. A Mini Review on Superhydrophobic and Transparent Surfaces. *Chem. Rec.* **2020**, *20*, 1257−1268.

(5) Miao, S.; Xiong, Z.; Zhang, J.; Wu, Y.; Gong, X. Polydopamine/$SiO_2$ Hybrid Structured Superamphiphobic Fabrics with Good Photothermal Behavior. *Langmuir* **2022**, *38*, 9431−9440.

(6) Xiong, Z.; Yu, H.; Gong, X. Designing Photothermal Superhydrophobic PET Fabrics via In Situ Polymerization and 1,4-Conjugation Addition Reaction. *Langmuir* **2022**, *38*, 8708−8718.

(7) Han, X.; Gong, X. In Situ, One-Pot Method to Prepare Robust Superamphiphobic Cotton Fabrics for High Buoyancy and Good Antifouling. *ACS Appl. Mater. Interfaces* **2021**, *13*, 31298−31309.

(8) Shrey, S.; Mokhtari, M.; Farmer, W. R. *Modifying Proppant Surface with Nano-Roughness Coating to Enhance Fracture Conductivity*, SPE-191826-18ERM-MS..
(9) Wong, T. I.; Wang, H.; Wang, F.; Sin, S. L.; Quan, C. G.; Wang, S. J.; Zhou, X. Development of a Highly Transparent Super-amphiphobic Plastic Sheet by Nanoparticle and Chemical Coating. *J. Colloid Interface Sci.* **2016**, *467*, 245−252.
(10) Yu, X.; Shi, X.; Xue, F.; Bai, W.; Li, Y.; Liu, Y.; Feng, L. SiO2 Nanoparticle-Containing Superhydrophobic Materials with Enhanced Durability via Facile and Scalable Spray Method. *Colloids Surf., A* **2021**, *626*, No. 127014.
(11) Sigmund, W.; Hung, Y. C. Transparent Durable Super-hydrophobic Ceramic Coating, US20170058131A1, 2016.
(12) Lee, S. G.; Ham, D. S.; Lee, D. Y.; Bong, H.; Cho, K. Transparent Superhydrophobic/Translucent Superamphiphobic Coatings Based on Silica-Fluoropolymer Hybrid Nanoparticles. *Langmuir* **2013**, *29*, 15051−15057.
(13) Zhang, J.; Liu, S.; Huang, Y.; Lv, Y.; Kong, M.; Li, G. Durable Fluorinated-$SiO_2$/Epoxy Superhydrophobic Coatings on Polycarbonate with Strong Interfacial Adhesion Enhanced by Solvent-Induced Crystallization. *Prog. Org. Coat.* **2021**, *150*, No. 106002.
(14) Ke, C.; Zhang, C.; Wu, X.; Jiang, Y. Highly Transparent and Robust Superhydrophobic Coatings Fabricated via a Facile Sol-Gel Process. *Thin Solid Films* **2021**, *723*, No. 138583.
(15) Radwan, A. B.; Mohamed, A. M. A.; Abdullah, A. M.; Al-Maadeed, M. A. Corrosion Protection of Electrospun PVDF−ZnO Superhydrophobic Coating. *Surf. Coat. Technol.* **2016**, *289*, 136−143.
(16) Tombesi, A.; Li, S.; Sathasivam, S.; Page, K.; Heale, F. L.; Pettinari, C.; Carmalt, C. J.; Parkin, I. P. Aerosol-Assisted Chemical Vapor Deposition of Transparent Superhydrophobic Film by Using Mixed Functional Alkoxysilanes. *Sci. Rep.* **2019**, *9*, 7549.
(17) Nguyen, T.; Wortman, P.; He, Z.; Goulas, J.; Yan, H.; Mokhtari, M.; Zhou, X. D.; Fei, L. Achieving Superhydrophobic Surfaces via Air-Assisted Electrospray. *Langmuir* **2022**, *38*, 2852−2861.
(18) Deng, X.; Mammen, L.; Butt, H. J.; Vollmer, D. Candle Soot as a Template for a Transparent Robust Superamphiphobic Coating. *Science* **2012**, *335*, 67−70.
(19) Zhu, X.; Zhang, Z.; Ren, G.; Men, X.; Ge, B.; Zhou, X. Designing Transparent Superamphiphobic Coatings Directed by Carbon Nanotubes. *J. Colloid Interface Sci.* **2014**, *421*, 141−145.
(20) Zhang, F.; Qian, H.; Wang, L.; Wang, Z.; Du, C.; Li, X.; Zhang, D. Superhydrophobic Carbon Nanotubes/Epoxy Nanocomposite Coating by Facile One-Step Spraying. *Surf. Coat. Technol.* **2018**, *341*, 15−23.
(21) Mokarian, Z.; Rasuli, R.; Abedini, Y. Facile Synthesis of Stable Superhydrophobic Nanocomposite Based on Multi-Walled Carbon Nanotubes. *Appl. Surf. Sci.* **2016**, *369*, 567−575.
(22) Li, B.; Zhang, J. Polysiloxane/Multiwalled Carbon Nanotubes Nanocomposites and Their Applications as Ultrastable Healable and Superhydrophobic Coatings. *Carbon* **2015**, *93*, 648−658.
(23) Ibrahim, I. A. M.; Zikry, A. A. F.; Sharaf, M. A.; Zikry, A. Preparation of Spherical Silica Nanoparticles: Stober Silica. *J. Am. Sci.* **2010**, *6*, 985−989.
(24) Xu, Y.; Liu, R.; Wu, D.; Sun, Y.; Gao, H.; Yuan, H.; Deng, F. Ammonia-Catalyzed Hydrolysis Kinetics of Mixture of Tetraethoxysilane with Methyltriethoxysilane by 29Si NMR. *J. Non-Cryst. Solids* **2005**, *351*, 2403−2413.
(25) Adachi, T.; Sakka, S. The Role of N,N-Dimethylformamide, a DCCA, in the Formation of Silica Gel Monoliths by Sol-Gel Method. *J. Non-Cryst. Solids* **1988**, *99*, 118−128.
(26) Matsoukas, T.; Gulari, E. Dynamics of Growth of Silica Particles from Ammonia-Catalyzed Hydrolysis of Tetra-Ethyl-Orthosilicate. *J. Colloid Interface Sci.* **1988**, *124*, 252−261.
(27) Matsoukas, T.; Gulari, E. Monomer-Addition Growth with a Slow Initiation Step: A Growth Model for Silica Particles from Alkoxides. *J. Colloid Interface Sci.* **1989**, *132*, 13−21.
(28) Bogush, G. H.; Tracy, M. A.; Zukoski, C. F., IV Preparation of Monodisperse Silica Particles: Control of Size and Mass Fraction. *J. Non-Cryst. Solids* **1988**, *104*, 95−106.
(29) Bogush, G. H.; Zukoski, C. F., IV Studies of the Kinetics of the Precipitation of Uniform Silica Particles through the Hydrolysis and Condensation of Silicon Alkoxides. *J. Colloid Interface Sci.* **1991**, *142*, 1−18.
(30) Rahman, I. A.; Padavettan, V. Synthesis of Silica Nanoparticles by Sol-Gel: Size-Dependent Properties Surface Modification, and Applications in Silica-Polymer Nanocomposites a Review. *J. Nanomater.* **2012**, *2012*, No. 132424.
(31) Van Blaaderen, A.; van Geest, J.; Vrij, A. Monodisperse Colloidal Silica Spheres from Tetraalkoxysilanes: Particle Formation and Growth Mechanism. *J. Colloid Interface Sci.* **1992**, *154*, 481−501.
(32) Lee, K.; Sathyagal, A. N.; McCormick, A. V. A Closer Look at an Aggregation Model of the Stöber Process. *Colloids Surf., A* **1998**, *144*, 115−125.
(33) Heiman-Burstein, D.; Dotan, A.; Dodiuk, H.; Kenig, S. Hybrid Sol-Gel Superhydrophobic Coatings Based on Alkyl Silane-Modified Nanosilica. *Polymers* **2021**, *13*, 1−15.
(34) Zhang, Z. Y.; Wang, W. L.; Korpacz, A. N.; Dufour, C. R.; Weiland, Z. J.; Lambert, C. R.; Timko, M. T. Binary Liquid Mixture Contact-Angle Measurements for Precise Estimation of Surface Free Energy. *Langmuir* **2019**, *35*, 12317−12325.




https://doi.org/10.1021/acs.langmuir.3c00233
*Langmuir* 2023, 39, 5495−5504